

Large-composition-range pure-phase homogeneous InAs_{1-x}Sb_x nanowires

Lianjun Wen,^{†,‡} Dong Pan,^{*,†,‡,⊥} Lei Liu,^{†,‡} Shucheng Tong,[†] Ran Zhuo,^{†,‡} and Jianhua
Zhao^{*,†,‡,§}

[†]*State Key Laboratory of Superlattices and Microstructures, Institute of Semiconductors, Chinese
Academy of Sciences, P.O. Box 912, Beijing 100083, China*

[‡]*College of Materials Science and Opto-Electronic Technology, University of Chinese Academy of
Sciences, Beijing 100049, China*

[⊥]*Beijing Academy of Quantum Information Sciences, 100193 Beijing, China*

[§]*CAS Center for Excellence in Topological Quantum Computation, University of Chinese
Academy of Sciences, Beijing 100049, China*

(Dated: November 3, 2021)

Narrow bandgap InAs_{1-x}Sb_x nanowires show broad prospects for applications in wide spectrum infrared detectors, high-performance transistors and quantum computation. Realizing such applications require the fine control of composition and crystal structure of nanowires. However, to date, the fabrication of large-composition-range pure-phase homogeneous InAs_{1-x}Sb_x nanowires remains a huge challenge. Here, we first report the growth of large-composition-range stemless InAs_{1-x}Sb_x nanowires ($0 \leq x \leq 0.63$) on Si (111) substrates by molecular-beam epitaxy. It is found that pure-phase InAs_{1-x}Sb_x nanowires can be successfully obtained by controlling the antimony content x , nanowire diameter and nanowire growth direction. Detailed EDS data show that the antimony is uniformly distributed along the axial and radial directions of InAs_{1-x}Sb_x nanowires and no spontaneous core-shell nanostructures form in the nanowires. Based on field-effect measurements, we confirm that InAs_{1-x}Sb_x nanowires exhibit good conductivity and their mobilities can be up to $4200 \text{ cm}^2\text{V}^{-1}\text{s}^{-1}$ at 7 K. Our work lays the foundation for the development of InAs_{1-x}Sb_x nanowire optoelectronic, electronic and quantum devices.

*E-mails: pandong@semi.ac.cn; jhzhao@semi.ac.cn

Ternary III-V nanowires, whose properties can be tuned and designed through varying composition, have aroused tremendous research interest in recent years.¹⁻⁹ Among them, InAs_{1-x}Sb_x nanowires are of particular interest due to their tunable narrow bandgaps (0.1 ~ 0.4 eV), high electron mobilities, strong spin-orbit interactions and large g-factors.¹⁰⁻¹⁵ These unique properties make them an ideal platform for studying wide spectrum infrared detectors, high-speed transistors and topological physics.^{2, 7-11, 16-20} To realize these applications, much work has been done to grow InAs_{1-x}Sb_x nanowires on various substrates by chemical vapor deposition, metal-organic vapor phase epitaxy, chemical beam epitaxy and molecular-beam epitaxy (MBE).^{9, 14, 21-32} Nevertheless, there are still many unsolved problems related to the controllable growth of InAs_{1-x}Sb_x nanowires.^{21, 24-25, 33} On one hand, to date, it is still difficult to fabricate stemless InAs_{1-x}Sb_x nanowires with higher antimony contents ($x > 0.35$).²⁵ On the other hand, these nanowires typically exhibit random mixtures of zinc-blende (ZB) and wurtzite (WZ) phases.^{21, 23-26} High-density planar defects, such as stacking fault (SF), rotational twin and grain boundary (GB), are usually found in these nanowires. Such defects can degrade their optical and electrical properties.³⁴⁻³⁵ Furthermore, the unevenly compositional distribution has also been found in InAs_{1-x}Sb_x nanowires, and even the spontaneous core-shell structure is always observed.^{9, 20, 25, 33} These unexpected results are hindering the research of bandgap engineering and topological physics based on InAs_{1-x}Sb_x nanowires.³⁵⁻³⁶ To the best of our knowledge, up to now, the fabrication of large-composition-range pure-phase stemless InAs_{1-x}Sb_x nanowires with homogeneous compositional distribution has not been realized yet.

In this work, we demonstrate the growth of large-composition-range pure-phase InAs₁₋

_xSb_x nanowires ($0 \leq x \leq 0.63$) on Si (111) substrates using silver as catalysts by MBE. Detail structural studies confirm that pure WZ or ZB phase InAs_{1-x}Sb_x nanowires can be obtained by controlling the antimony content, nanowire diameter and nanowire growth direction. Energy dispersive spectrum (EDS) analyses verify that the antimony is uniformly distributed throughout the nanowire. Electrical measurements show that the grown InAs_{1-x}Sb_x nanowires exhibit a high electron mobility.

Large-range antimony content tunable. As mentioned above, so far, it is still difficult to prepare large-composition-range stemless InAs_{1-x}Sb_x nanowires no matter what the growth manners (foreign-catalyst-free or gold-assisted) were used.^{9, 21, 24-25, 29, 33} To resolve this problem, here we choose silver as catalysts to grow InAs_{1-x}Sb_x nanowires. We find that large-composition-range InAs_{1-x}Sb_x nanowires ($0 \leq x \leq 0.63$) can be successfully grown directly on Si (111) substrates by tuning the antimony flux (P_{Sb}). As shown in Figure 1a, with increasing P_{Sb} , more antimony atoms can be incorporated into nanowires, thereby obtaining nanowires with higher antimony contents (the corresponding scanning electron microscope (SEM) images can be found in Figure S1 in the supporting information). The antimony content x can be tuned from 0 to 0.63, which is approximately twice comparing with the previously reported results ($0 \leq x \leq 0.35$).^{9, 25} We also note that the antimony content x gradually becomes saturated with the increase of the P_{Sb} (see Figure 1a). Meanwhile, the density of nanowires begins to decrease (see Figure S1). Therefore, it is difficult to obtain InAs_{1-x}Sb_x nanowires with the antimony content x higher than 0.7.

It is well known that the surfactant effect of antimony plays an important role in the growth of III-Sb nanowires.^{4, 14, 21, 24-25, 37-38} It often enhances the lateral growth and inhibits

the axial growth of nanowires, which makes nanowires typically show a low aspect ratio (AR) (~ 10). However, we find that our $\text{InAs}_{1-x}\text{Sb}_x$ nanowires still exhibit an ultrahigh AR (> 30) although the surfactant effect of antimony cannot be avoided during nanowire growth. Figure 1b shows a curve of the average diameter and length of $\text{InAs}_{1-x}\text{Sb}_x$ nanowires as a function of the antimony content x (the average diameter is defined as the average of the diameter of the bottom of the nanowire and the diameter of the top of the nanowire). We can see that all $\text{InAs}_{1-x}\text{Sb}_x$ nanowires ($0 \leq x \leq 0.63$) show small diameter (10 ~ 80 nm) and ultrahigh AR (> 30), which is beneficial for quantum device research.³⁹ It can also be seen that as the antimony content x increases, due to the surfactant effect of antimony, the average diameter and length of nanowires begin to increase and decrease, respectively. The nanowires with a lower antimony content ($x \leq 0.3$) exhibit an ultrahigh AR of over 50, which is 2-4 times higher than the results of foreign-catalyst-free $\text{InAs}_{1-x}\text{Sb}_x$ nanowires.^{21, 25, 27, 33}

Crystal structure and phase purity control.

III-V nanowires typically exhibit a mixture of WZ and ZB phases, and a large number of planar defects usually formed in nanowires.^{21, 24-26} Similar results are also observed in our $\text{InAs}_{1-x}\text{Sb}_x$ nanowires with low antimony content ($x < 0.2$). As shown in Figure 2a,b, GBs and SFs can be easily found along the axial direction of nanowires. Such defects will degrade the properties of nanowire devices, so the realization of pure-phase $\text{InAs}_{1-x}\text{Sb}_x$ nanowires is of great significance.³⁵ Based on detailed structural studies, we find that pure ZB phase $\text{InAs}_{1-x}\text{Sb}_x$ nanowires can be achieved by further increasing the antimony content x . Figure 2 shows high resolution transmission electron microscope (HRTEM) images and corresponding selected area electron diffraction (SAED) patterns of $\langle 0001 \rangle$ - or

$\langle 111 \rangle$ -oriented $\text{InAs}_{1-x}\text{Sb}_x$ nanowires. To minimize the effect of nanowire diameter on its crystal structure, the nanowire diameter shown here is fixed in the range from 31 nm to 54 nm. It can be easily found from Figure 2 that the phase purity of $\text{InAs}_{1-x}\text{Sb}_x$ nanowires depends on the antimony content x . With the increase of the antimony content x , the favorable phase of nanowires gradually changes from WZ to ZB (see Figure 2g-l). When the antimony content x exceeds 0.25 (see Figure 2c-f), all nanowires exhibit a pure ZB phase. These results indicate that the fine control of antimony content is an effective method to grow pure-phase $\text{InAs}_{1-x}\text{Sb}_x$ nanowires.

As shown in Figure 2, there are always a large number of defects in $\text{InAs}_{1-x}\text{Sb}_x$ nanowires with the antimony content x less than 0.2. For many potential applications, such as wide spectrum infrared detectors, it is also important to prepare pure-phase nanowires with low antimony content ($x < 0.2$).^{6, 25, 31, 36} As shown in Figure 3, we find that pure-phase $\text{InAs}_{1-x}\text{Sb}_x$ nanowires ($0 \leq x \leq 0.63$) can be achieved by controlling their diameters or growth directions. It can be seen from Figure 3a that the $\langle 0001 \rangle$ -oriented $\text{InAs}_{0.93}\text{Sb}_{0.07}$ nanowire with a diameter of 13 nm exhibits pure WZ phase. And the density of planar defects in this nanowire can be as low as $10 \mu\text{m}^{-1}$. It indicates that reducing the diameter can effectively improve the phase purity of $\text{InAs}_{1-x}\text{Sb}_x$ nanowires with a low antimony content. However, this method may not be suitable for nanowires with higher antimony contents. The reasons are as follows: 1) it is difficult to obtain ultrathin nanowires due to the surfactant effect of antimony (see Figure 1b); 2) ZB phase becomes the dominant phase as x increases (see Figure 2). Figure 3b-f shows the HRTEM images and corresponding SAED patterns of $\text{InAs}_{1-x}\text{Sb}_x$ nanowires grown along non- $\langle 111 \rangle$ directions. It can be seen that all the $\text{InAs}_{1-x}\text{Sb}_x$ nanowires with different antimony contents

grown along $\langle 100 \rangle$, $\langle 110 \rangle$ and $\langle 112 \rangle$ directions exhibit pure ZB phase (see Figure 3b-f). Similar results have also been found in InAs nanowires.^{15, 39-42} It indicates that the control of the growth direction of nanowires is also effective way to obtain pure-phase $\text{InAs}_{1-x}\text{Sb}_x$ nanowires. This method may be easy to implement by using substrates with different crystallographic orientations.³² Above results confirm that pure-phase $\text{InAs}_{1-x}\text{Sb}_x$ nanowires with a large-composition-range ($0 \leq x \leq 0.63$) can be successfully fabricated by MBE.

Homogeneous compositional distribution. In addition to the control of phase purity, the effective control of compositional distribution of ternary nanowires is also very important for tuning their properties. As mentioned above, the unevenly compositional distribution has always been found in $\text{InAs}_{1-x}\text{Sb}_x$ nanowires.^{9, 20, 25, 33} However, based on detailed EDS analyses, we find that indium, arsenic and antimony are uniformly distributed in our $\text{InAs}_{1-x}\text{Sb}_x$ nanowires, and no spontaneous core-shell nanostructures are found. Figure 4 shows high-angle annular dark field scanning transmission electron microscope (HAADF-STEM) images and EDS data of $\text{InAs}_{1-x}\text{Sb}_x$ nanowires with different antimony contents. We can see from Figure 4a₀-f₄ that indium, arsenic and antimony are uniformly distributed for all $\text{InAs}_{1-x}\text{Sb}_x$ nanowires. It is also worth noting that the compositional distribution near the catalyst-nanowire interface exhibits slight inhomogeneity due to the reservoir effect of catalyst (this phenomenon has been discussed in detail in our previous article).³² In addition, silver-indium catalyst segregation^{32, 43} is suppressed with increasing x , which may be related to antimony residues in the catalyst nanoparticle. The quantitative EDS data indicate that there are higher antimony residues in the catalyst nanoparticle for those nanowires with a higher antimony content. The high

antimony residues can lower the surface energy of the catalyst nanoparticle,^{14, 32, 43-44} which makes it stable in the air.

Figure 4g₀ is a cross section HAADF-STEM image of the $\text{InAs}_{0.71}\text{Sb}_{0.29}$ nanowire, which shows that the nanowire has the hexagonal cross section (more details available in S2 in the supporting information). We can see from Figure 4g₁-4h that the distribution of indium, arsenic and antimony is uniform across the cross section of the nanowire, and no obvious core-shell nanostructures formed. From Figure 4g₂, it can be found that the cross section of the EDS maps of antimony is slightly larger than that of arsenic. This phenomenon may be related to the formation of a native oxide layer (see Figure 4g₃,h). Quantitative EDS data prove that the variation of the antimony content x on the cross section is less than 2%. Our results are different from those of foreign-catalyst-free or gold-assisted nanowires, where the antimony distribution on the cross section is significantly heterogeneous, and even the spontaneous core-shell structure can be found.^{9, 20, 25, 33} In those works, $\text{InAs}_{1-x}\text{Sb}_x$ nanowires show a larger diameter (typically 100 ~ 200 nm) due to the strong vapor-solid growth on the sidewalls of nanowires. In contrast, our nanowires show a smaller diameter (typically 20 ~ 60 nm), and no obvious vapor-solid growth is observed on the sidewalls of nanowire. These results indicate that a small nanowire diameter may be the key to obtain homogeneous $\text{InAs}_{1-x}\text{Sb}_x$ nanowires.

Electrical properties of $\text{InAs}_{1-x}\text{Sb}_x$ nanowires. We evaluate the electrical properties of as-grown $\text{InAs}_{1-x}\text{Sb}_x$ nanowires using back-gated field-effect transistor (FET) devices. The schematic diagram and SEM image of the $\text{InAs}_{1-x}\text{Sb}_x$ nanowire device are presented in Figure 5a. In this device, the bias voltage (V_{ds}) is applied to the drain electrode, the source electrode is grounded, and the back-

gate voltage (V_g) is used to tune the carrier concentration of the nanowire. Figure 5b shows the output characteristics of $\text{InAs}_{0.93}\text{Sb}_{0.07}$ nanowire FETs at 300 K with different V_g . It can be seen that the device shows good linear shape and current saturation, which suggests the ohmic contact of the device. We use $\sigma = \frac{4GL}{\pi D^2}$ to extract the conductivity σ of nanowires, where G is the conductance, L is the distance between the contacts and D is the diameter of nanowire. As shown in Figure 5c, it can be found that $\text{InAs}_{1-x}\text{Sb}_x$ nanowires with higher antimony content show better conductivity for $x \leq 0.29$, which is consistent with the reported results of foreign-catalyst-free nanowires.^{21, 25} For $x \geq 0.29$, the average conductivity of nanowires is independent of the antimony content x , which may be related to the fact that they have substantially the same bandgap at room temperature.¹¹

Figure 5d shows the typical transfer characteristics of $\text{InAs}_{1-x}\text{Sb}_x$ FETs with different antimony contents at $V_{ds} = 100$ mV. It can be seen that all devices exhibit n-type conduction. The on-off ratios of these devices range from 4 to 22, which indicates $\text{InAs}_{1-x}\text{Sb}_x$ nanowires cannot be turned off completely at 300 K due to their narrow bandgaps.^{11, 21, 45} The field-effect mobility of nanowires can be estimated using $\mu = \frac{g_m L^2}{C V_{ds}}$, where g_m is transconductance and C is nanowire-gate capacitance. For back-gated FETs, the nanowire-gate capacitance can be approximated by $C = \frac{2\pi\epsilon_0\epsilon_r L}{\cosh^{-1}(1 + \frac{2t_{ox}}{D})}$, where ϵ_0 is permittivity, ϵ_r is relative permittivity and t_{ox} is the thickness of the dielectric layer.⁴⁶ Using the estimated conductivity and mobility, the carrier concentration n can also be calculated by $n = \frac{\sigma}{e\mu}$, where e is the elementary charge. As shown in Figure 5e, the average mobility of

nanowires first increases with the increase of the antimony content, and then tends to be saturated for $x \geq 0.29$. The carrier concentration n varies slightly with the antimony content (see Figure 5f). The maximum mobility (μ_m) of nanowires at 300 K can reach $1400 \text{ cm}^2\text{V}^{-1}\text{s}^{-1}$, which demonstrates high-quality $\text{InAs}_{1-x}\text{Sb}_x$ nanowires have been grown by MBE using silver catalysts.

Figure 6 shows the output and transfer characteristics of $\text{InAs}_{1-x}\text{Sb}_x$ nanowire FETs at 7 K. We can see that these devices still present good ohmic contacts (see Figure 6a), and most $\text{InAs}_{1-x}\text{Sb}_x$ FETs exhibit n-type conduction (see Figure 6b). Different from the results at 300 K, these devices show higher on-off ratios ($10^3 \sim 10^4$) at 7 K, which suggests the carrier concentration in the junction region can be effectively tuned by V_g . In addition, ambipolar behavior is observed in some $\text{InAs}_{1-x}\text{Sb}_x$ nanowires ($x \geq 0.39$). As shown in Figure 6c, as the V_g becomes more negative, the conduction type of the $\text{InAs}_{0.44}\text{Sb}_{0.56}$ nanowire FET changes from n-type to p-type. Ambipolar behavior is usually found in narrow bandgap nanowires, which can be explained by band-to-band tunneling mechanism.⁴⁷⁻⁵¹ At large negative V_g , the tunneling of hole from the valence band in the junction region to the conduction band in the electrode region results in the formation of a reverse current.

Based on the output and transfer characteristics of nanowire FETs, the mobility and carrier concentration of nanowires at 7 K are also extracted. We can see from Figure 6d that the mobility of nanowires at 7 K increases approximately 3 times compared to the results at room temperature. This is because phonon scattering is significantly suppressed at low temperatures, thereby increasing the mobility of the nanowires. The trend of the mobility varying with the antimony content x at 7 K is similar to that at 300 K, and the maximum mobility of $\text{InAs}_{1-x}\text{Sb}_x$ nanowires with a

diameter of 40 ~ 70 nm can be up to 4200 $\text{cm}^2\text{V}^{-1}\text{s}^{-1}$. The estimated mobility of our $\text{InAs}_{1-x}\text{Sb}_x$ nanowires is comparable to that of $\text{InAs}_{0.3}\text{Sb}_{0.7}/\text{Sn}$ semiconductor-superconductor nanowires ($\text{InAs}_{0.3}\text{Sb}_{0.7}$ nanowires grown on InAs nanowire stems using gold as catalysts), which suggests our nanowires have great potential for achieving high-quality hybrid semiconductor-superconductor nanowire devices.² As shown in Figure 6e, unexpectedly, $\text{InAs}_{0.93}\text{Sb}_{0.07}$ nanowires show slightly higher carrier concentration than other $\text{InAs}_{1-x}\text{Sb}_x$ nanowires ($x \geq 0.13$). It may be understood by the diameter-dependent electrical transport properties of nanowires.^{40, 52-53} We can see from Figure 6f that $\text{InAs}_{1-x}\text{Sb}_x$ nanowires with the smaller diameter exhibit higher carrier concentration (especially for $D < 30$ nm). Similar phenomena have also been observed in InAs nanowires, where nanowires with a smaller diameter show higher carrier concentration due to the presence of a surface accumulation layer.^{40, 52-53} As a result, in our case, it can be inferred that the surface accumulation layer of $\text{InAs}_{0.93}\text{Sb}_{0.07}$ nanowires can contribute more carriers due to their smaller diameters, which makes their carrier concentration higher than that of other samples (see Figure 6f).

In summary, we demonstrate the growth of large-composition-range stemless $\text{InAs}_{1-x}\text{Sb}_x$ nanowires on Si (111) substrates by MBE for the first time. The antimony content x can be tuned from 0 to 0.63, which is about two times larger than the previous experiments ($0 \leq x \leq 0.35$). Furthermore, we also realize the control of phase purity of $\text{InAs}_{1-x}\text{Sb}_x$ nanowires. Pure-phase $\text{InAs}_{1-x}\text{Sb}_x$ nanowires have been achieved by increasing the antimony content, reducing the nanowire diameter and growing nanowires along non- $\langle 111 \rangle$ directions. In particular, we resolve the problem of uneven compositional distribution of $\text{InAs}_{1-x}\text{Sb}_x$ nanowires. Detailed EDS analyses confirm that

the antimony is uniformly distributed along the axial and radial directions of $\text{InAs}_{1-x}\text{Sb}_x$ nanowires, and no spontaneous core-shell nanostructures are found. In addition, electrical measurements confirm that our $\text{InAs}_{1-x}\text{Sb}_x$ nanowires have high mobilities, which further prove that the nanowires have high crystal quality. Our work paves the way toward future high-performance $\text{InAs}_{1-x}\text{Sb}_x$ nanowire electronic, optoelectronic and quantum devices.

EXPERIMENTAL METHOD

Nanowire Growth. All silver-assisted $\text{InAs}_{1-x}\text{Sb}_x$ nanowires were grown in a solid source MBE system (VG V80H) on Si (111) substrates. Before loading the Si (111) substrate into the MBE chamber, a diluted HF (2%) solution was used to remove its surface contamination and native oxide layer. Prior to nanowire growth, the silver layer with a nominal thickness of less than 0.5 nm was deposited at room temperature and then annealed in situ at 600 °C under constant arsenic flux to generate silver catalyst nanoparticles. The nanowire growth was started by opening indium and antimony shutters simultaneously when the growth temperature reached 505 °C. To obtain $\text{InAs}_{1-x}\text{Sb}_x$ nanowires with different antimony contents, the indium and arsenic fluxes were fixed at 1.6×10^{-7} mbar and 1.6×10^{-6} mbar, respectively, while the antimony flux was changed from 1.3×10^{-7} mbar to 6.4×10^{-6} mbar. The nanowire growth lasts 40 minutes. The morphology and crystal structure of $\text{InAs}_{1-x}\text{Sb}_x$ nanowires were investigated by a FEI NanoSEM 650 scanning electron microscope and a JEM F200 transmission electron microscope, respectively. In the JEM F200 system, the compositional distribution of nanowires was also measured by EDS during HAADF-STEM observations.

Device Fabrication. For the electrical characterizations of $\text{InAs}_{1-x}\text{Sb}_x$ nanowires, the back-gated FETs were fabricated. The as-grown nanowires were firstly transferred to a highly p-doped Si (100) substrate covered with a 300 nm thermal oxide layer. Then, the metal electrodes were attached by the standard electron beam lithography process. Before

depositing metal, a diluted $(\text{NH}_4)_2\text{S}_x$ solution was used to remove the native oxide layer of nanowires in the contact areas. After that, a chromium/gold (20 nm/80 nm) film was evaporated followed by lift-off in acetone. All electrical measurements of nanowire devices were performed on a probe station using a semiconductor parameter analyzer.

ACKNOWLEDGMENTS

This work was supported by the National Natural Science Foundation of China (grant nos. 61974138 and 92065106), Beijing Natural Science Foundation (grant no. 1192017) and the Strategic Priority Research Program of Chinese Academy of Sciences (Grant No. XDB28000000). D.P. also acknowledges the support from Youth Innovation Promotion Association, Chinese Academy of Sciences (no. 2017156).

NOTES

The authors declare that they have no competing financial interests.

REFERENCES

- (1) Tomioka, K.; Yoshimura, M.; Fukui, T. A III-V Nanowire Channel on Silicon for High-Performance Vertical Transistors. *Nature* **2012**, *488*, 189-192.
- (2) Khan, S. A.; Lampadaris, C.; Cui, J.; Stampfer, L.; Liu, Y.; Pauka, S. J.; Cachaza, M. E.; Fiordaliso, E. M.; Kang, J. H.; Korneychuk, S.; Mutas, T.; Sestoft, J. E.; Krizek, F.; Tanta, R.; Cassidy, M. C.; Jespersen, T. S.; Krogstrup, P. Highly Transparent Gatable Superconducting Shadow Junctions. *ACS Nano* **2020**, *14*, 14605-14615.
- (3) Ghasemi, M.; Leshchenko, E. D.; Johansson, J. Assembling Your Nanowire: an Overview of Composition Tuning in Ternary III-V Nanowires. *Nanotechnology* **2021**, *32*, 072001.
- (4) Li, L. X.; Pan, D.; Xue, Y. Z.; Wang, X. L.; Lin, M. L.; Su, D.; Zhang, Q. L.; Yu, X. Z.; So, H.; Wei, D. H.; Sun, B. Q.; Tan, P. H.; Pan, A. L.; Zhao, J. H. Near Full-Composition-Range High-Quality $\text{GaAs}_{1-x}\text{Sb}_x$ Nanowires Grown by Molecular-Beam Epitaxy. *Nano Lett.* **2017**, *17*, 622-630.
- (5) Dubrovskii, V. G. Understanding the Vapor-Liquid-

Solid Growth and Composition of Ternary III-V Nanowires and Nanowire Heterostructures. *J. Phys. D Appl. Phys.* **2017**, *50*, 453001.

- (6) Xu, T. F.; Wang, H. L.; Chen, X. Y.; Luo, M.; Zhang, L. L.; Wang, Y. M.; Chen, F. S.; Shan, C. X.; Yu, C. H. Recent Progress on Infrared Photodetectors Based on InAs and InAsSb Nanowires. *Nanotechnology* **2020**, *31*, 294004.

- (7) Ren, D.; Azizur-Rahman, K. M.; Rong, Z.; Juang, B. C.; Somasundaram, S.; Shahili, M.; Farrell, A. C.; Williams, B. S.; Huffaker, D. L. Room-Temperature Midwavelength Infrared InAsSb Nanowire Photodetector Arrays with Al_2O_3 Passivation. *Nano Lett.* **2019**, *19*, 2793-2802.

- (8) Sestoft, J. E.; Kanne, T.; Gejl, A. N.; von Soosten, M.; Yodh, J. S.; Sherman, D.; Tarasinski, B.; Wimmer, M.; Johnson, E.; Deng, M.; Nygard, J.; Jespersen, T. S.; Marcus, C. M.; Krogstrup, P. Engineering Hybrid Epitaxial InAsSb/Al Nanowires for Stronger Topological Protection. *Phys. Rev. Mater.* **2018**, *2*, 044202.

- (9) Yao, X. M.; Zhang, X. T.; Sun, Q.; Wei, D. D.; Chen, P. P.; Zou, J. Anomalous Photoelectrical Properties through Strain Engineering Based on a Single Bent InAsSb Nanowire. *ACS Appl. Mater. Inter.* **2021**, *13*, 5691-5698.

- (10) Fang, H.; Chuang, S.; Takei, K.; Kim, H. S.; Plis, E.; Liu, C. H.; Krishna, S.; Chueh, Y. L.; Javey, A. Ultrathin-Body High-Mobility InAsSb-on-Insulator Field-Effect Transistors. *IEEE Electr. Device Lett.* **2012**, *33*, 504-506.

- (11) Winkler, G. W.; Wu, Q. S.; Troyer, M.; Krogstrup, P.; Soluyanov, A. A. Topological Phases in $\text{InAs}_{1-x}\text{Sb}_x$: From Novel Topological Semimetal to Majorana Wire. *Phys. Rev. Lett.* **2016**, *117*, 076403.

- (12) Mayer, W.; Schiela, W. F.; Yuan, J.; Hatefipour, M.; Sarney, W. L.; Svensson, S. P.; Leff, A. C.; Campos, T.; Wickramasinghe, K. S.; Dartiailh, M. C.; Zutic, I.; Shabani, J. Superconducting Proximity Effect in InAsSb Surface Quantum Wells with In Situ Al Contacts. *ACS Appl. Electron. Mater.* **2020**, *2*, 2351-2356.

- (13) Zhuang, Q. D.; Alradhi, H.; Jin, Z. M.; Chen, X. R.; Shao, J.; Chen, X.; Sanchez, A. M.; Cao, Y. C.; Liu,

- J. Y.; Yates, P.; Durose, K.; Jin, C. J. Optically Efficient InAsSb Nanowires for Silicon-Based Mid-Wavelength Infrared Optoelectronics. *Nanotechnology* **2017**, *28*, 105710.
- (14) Anyebe, E. A.; Rajpalke, M. K.; Veal, T. D.; Jin, C. J.; Wang, Z. M.; Zhuang, Q. D. Surfactant Effect of Antimony Addition to the Morphology of Self-Catalyzed InAs_{1-x}Sb_x Nanowires. *Nano Res.* **2015**, *8*, 1309-1319.
- (15) Pan, D.; Fu, M. Q.; Yu, X. Z.; Wang, X. L.; Zhu, L. J.; Nie, S. H.; Wang, S. L.; Chen, Q.; Xiong, P.; von Molnar, S.; Zhao, J. H. Controlled Synthesis of Phase-Pure InAs Nanowires on Si(111) by Diminishing the Diameter to 10 nm. *Nano Lett.* **2014**, *14*, 1214-1220.
- (16) Oreg, Y.; Refael, G.; von Oppen, F. Helical Liquids and Majorana Bound States in Quantum Wires. *Phys. Rev. Lett.* **2010**, *105*, 177002.
- (17) Lutchyn, R. M.; Sau, J. D.; Das Sarma, S. Majorana Fermions and a Topological Phase Transition in Semiconductor-Superconductor Heterostructures. *Phys. Rev. Lett.* **2010**, *105*, 077001.
- (18) Sau, J. D.; Lutchyn, R. M.; Tewari, S.; Das Sarma, S. Generic New Platform for Topological Quantum Computation Using Semiconductor Heterostructures. *Phys. Rev. Lett.* **2010**, *104*, 040502.
- (19) Boland, J. L.; Amaduzzi, F.; Sterzl, S.; Potts, H.; Herz, L. M.; Morral, A. F. I.; Johnston, M. B. High Electron Mobility and Insights into Temperature-Dependent Scattering Mechanisms in InAsSb Nanowires. *Nano Lett.* **2018**, *18*, 3703-3710.
- (20) Robson, M.; Azizur-Rahman, K. M.; Parent, D.; Wojdylo, P.; Thompson, D. A.; LaPierre, R. R. Multispectral Absorptance from Large-Diameter InAsSb Nanowire Arrays in a Single Epitaxial Growth on Silicon. *Nano Futures* **2017**, *1*, 035001.
- (21) Sourribes, M. J. L.; Isakov, I.; Panfilova, M.; Liu, H. Y.; Warburton, P. A. Mobility Enhancement by Sb-mediated Minimisation of Stacking Fault Density in InAs Nanowires Grown on Silicon. *Nano Lett.* **2014**, *14*, 1643-1650.
- (22) Anyebe, E. A.; Zhuang, Q. Self-Catalysed InAs_{1-x}Sb_x Nanowires Grown Directly on Bare Si Substrates. *Mate. Res. Bull.* **2014**, *60*, 572-575.
- (23) Du, W. N.; Yang, X. G.; Wang, X. Y.; Pan, H. Y.; Ji, H. M.; Luo, S.; Yang, T.; Wang, Z. G. The Self-Seeded Growth of InAsSb Nanowires on Silicon by Metal-Organic Vapor Phase Epitaxy. *J. Cryst. Growth* **2014**, *396*, 33-37.
- (24) Zhuang, Q. D.; Anyebe, E. A.; Chen, R.; Liu, H.; Sanchez, A. M.; Rajpalke, M. K.; Veal, T. D.; Wang, Z. M.; Huang, Y. Z.; Sun, H. D. Sb-Induced Phase Control of InAsSb Nanowires Grown by Molecular Beam Epitaxy. *Nano Lett.* **2015**, *15*, 1109-1116.
- (25) Potts, H.; Friedl, M.; Amaduzzi, F.; Tang, K. C.; Tutuncuoglu, G.; Matteini, F.; Alarcon Llado, E.; McIntyre, P. C.; i Morral, A. F. From Twinning to Pure Zincblende Catalyst-Free InAs(Sb) Nanowires. *Nano Lett.* **2016**, *16*, 637-643.
- (26) Farrell, A. C.; Lee, W. J.; Senanayake, P.; Haddad, M. A.; Prikhodko, S. V.; Huffaker, D. L. High-Quality InAsSb Nanowires Grown by Catalyst-Free Selective-Area Metal-Organic Chemical Vapor Deposition. *Nano Lett.* **2015**, *15*, 6614-6619.
- (27) Anyebe, E. A.; Sanchez, A. M.; Hindmarsh, S.; Chen, X.; Shao, J.; Rajpalke, M. K.; Veal, T. D.; Robinson, B. J.; Kolosoy, O.; Anderson, F.; Sundaram, R.; Wang, Z. M.; Falko, V.; Zhuang, Q. Realization of Vertically Aligned, Ultrahigh Aspect Ratio InAsSb Nanowires on Graphite. *Nano Lett.* **2015**, *15*, 4348-4355.
- (28) Du, W. N.; Yang, X. G.; Pan, H. Y.; Wang, X. Y.; Ji, H. M.; Luo, S.; Ji, X. H.; Wang, Z. G.; Yang, T. Two Different Growth Mechanisms for Au-Free InAsSb Nanowires Growth on Si Substrate. *Cryst. Growth Des.* **2015**, *15*, 2413-2418.
- (29) Namazi, L.; Ghalamestani, S. G.; Lehmann, S.; Zamani, R. R.; Dick, K. A. Direct Nucleation, Morphology and Compositional Tuning of InAs_{1-x}Sb_x Nanowires on InAs (111) B Substrates. *Nanotechnology* **2017**, *28*, 165601.
- (30) Yang, X. G.; Du, W. N.; Ji, X. H.; Zhang, X. W.; Yang, T. Defect-Free InAsSb Nanowire Arrays on Si Substrates Grown by Selective-Area Metal-Organic Chemical Vapor Deposition. *Nanotechnology* **2018**, *29*, 405601.
- (31) Yip, S.; Li, D. P.; Li, F. Z.; Wang, W.; Kang, X. L.; Meng, Y.; Zhang, H.; Lai, Z. X.; Wang, F.; Ho, J. C. Unusual Phase-Pure Zinc Blende and Highly-

- Crystalline As-Rich InAs_{1-x}Sb_x Nanowires for High-Mobility Transistors. *J. Mater. Chem. C* **2020**, *8*, 13189-13196.
- (32) Wen, L. J.; Liu, L.; Liao, D. Y.; Zhuo, R.; Pan, D.; Zhao, J. H. Silver-Assisted Growth of High-Quality InAs_{1-x}Sb_x Nanowires by Molecular-beam Epitaxy. *Nanotechnology* **2020**, *31*, 465602.
- (33) Ruhstorfer, D.; Lang, A.; Matich, S.; Doblinger, M.; Riedl, H.; Finley, J. J.; Koblmüller, G. Growth Dynamics and Compositional Structure in Periodic InAsSb Nanowire Arrays on Si (111) Grown by Selective Area Molecular Beam Epitaxy. *Nanotechnology* **2021**, *32*, 135604.
- (34) Caroff, P.; Bolinsson, J.; Johansson, J. Crystal Phases in III-V Nanowires: From Random Toward Engineered Polytypism. *IEEE J. Sel. Top. Quant.* **2010**, *17*, 829-846.
- (35) Liu, J.; Potter, A. C.; Law, K. T.; Lee, P. A. Zero-Bias Peaks in the Tunneling Conductance of Spin-Orbit-Coupled Superconducting Wires with and without Majorana End-States. *Phys. Rev. Lett.* **2012**, *109*, 267002.
- (36) Takei, S.; Fregoso, B. M.; Hui, H. Y.; Lobos, A. M.; Das Sarma, S. Soft Superconducting Gap in Semiconductor Majorana Nanowires. *Phys. Rev. Lett.* **2013**, *110*, 186803.
- (37) Borg, B. M.; Wernersson, L. E. Synthesis and Properties of Antimonide Nanowires. *Nanotechnology* **2013**, *24*, 202001.
- (38) So, H.; Pan, D.; Li, L. X.; Zhao, J. H. Foreign-Catalyst-Free Growth of InAs/InSb Axial Heterostructure Nanowires on Si (111) by Molecular-Beam Epitaxy. *Nanotechnology* **2017**, *28*, 135704.
- (39) D. Pan; H. D. Song; S. Zhang; L. Liu; L. J. Wen; D. Y. Liao; R. Zhuo; Z. C. Wang; Z. T. Zhang; S. Yang; J. H. Ying; W. T. Miao; Y. Q. Li; R. N. Shang; H. Zhang; Zhao, J. H. In Situ Epitaxy of Pure Phase Ultra-Thin InAs-Al Nanowires for Quantum Devices. *arXiv preprint*, arXiv:2011.13620 2020.
- (40) Fu, M. Q.; Tang, Z. Q.; Li, X.; Ning, Z. Y.; Pan, D.; Zhao, J. H.; Wei, X. L.; Chen, Q. Crystal Phase- and Orientation-Dependent Electrical Transport Properties of InAs Nanowires. *Nano Lett.* **2016**, *16*, 2478-2484.
- (41) Xu, H.; Wang, Y.; Guo, Y.; Liao, Z.; Gao, Q.; Tan, H. H.; Jagadish, C.; Zou, J. Defect-Free <110> Zinc-blende Structured InAs Nanowires Catalyzed by Palladium. *Nano Lett.* **2012**, *12*, 5744.
- (42) Zhang, Z.; Zheng, K.; Lu, Z. Y.; Chen, P. P.; Lu, W.; Zou, J. Catalyst Orientation-Induced Growth of Defect-Free Zinc-Blende Structured <00 $\bar{1}$ > InAs Nanowires. *Nano Lett.* **2015**, *15*, 876-82.
- (43) Pan, D.; Wang, J. Y.; Zhang, W.; Zhu, L. J.; Su, X. J.; Fan, F. R.; Fu, Y. H.; Huang, S. Y.; Wei, D. H.; Zhang, L. J.; Sui, M. L.; Yartsev, A.; Xu, H. Q.; Zhao, J. H. Dimension Engineering of High-Quality InAs Nanostructures on a Wafer Scale. *Nano Lett.* **2019**, *19*, 1632-1642.
- (44) Aqra, F.; Ayyad, A. Surface Energies of Metals in Both Liquid and Solid States. *Appl. Surf. Sci.* **2011**, *257*, 6372-6379.
- (45) Nilsson, H. A.; Deng, M. T.; Caroff, P.; Thelander, C.; Samuelson, L.; Wernersson, L. E.; Xu, H. Q. InSb Nanowire Field-Effect Transistors and Quantum-Dot Devices. *IEEE J. Sel. Top. Quant.* **2011**, *17*, 907-914.
- (46) Wunnicke, O. Gate Capacitance of Back-Gated Nanowire Field-Effect Transistors. *Appl. Phys. Lett.* **2006**, *89*, 083102.
- (47) Nilsson, H. A.; Caroff, P.; Thelander, C.; Lind, E.; Karlstrom, O.; Wernersson, L. E. Temperature Dependent Properties of InSb and InAs Nanowire Field-Effect Transistors. *Appl. Phys. Lett.* **2010**, *96*, 153505.
- (48) Zhao, Y. J.; Candebat, D.; Delker, C.; Zi, Y. L.; Janes, D.; Appenzeller, J.; Yang, C. Understanding the Impact of Schottky Barriers on the Performance of Narrow Bandgap Nanowire Field Effect Transistors. *Nano Lett.* **2012**, *12*, 5331-5336.
- (49) Pan, D.; Fan, D. X.; Kang, N.; Zhi, J. H.; Yu, X. Z.; Xu, H. Q.; Zhao, J. H. Free-Standing Two-Dimensional Single-Crystalline InSb Nanosheets. *Nano Lett.* **2016**, *16*, 834-841.
- (50) Zhang, S. K.; Jiao, H. X.; Wang, X. D.; Chen, Y.; Wang, H. L.; Zhu, L. Q.; Jiang, W.; Liu, J. J.; Sun, L. X.; Lin, T.; Shen, H.; Hu, W. D.; Meng, X. J.; Pan, D.; Wang, J. L.; Zhao, J. H.; Chu, J. H. Highly Sensitive InSb Nanosheets Infrared Photodetector Passivated by Ferroelectric Polymer. *Adv. Funct. Mater.* **2020**, *30*, 2006156.

- (51) Fan, D. X.; Kang, N.; Ghalamestani, S. G.; Dick, K. A.; Xu, H. Q. Schottky barrier and contact resistance of InSb nanowire field-effect transistors. *Nanotechnology* **2016**, *27*, 275204.
- (52) Scheffler, M.; Nadj-Perge, S.; Kouwenhoven, L. P.; Borgstrom, M. T.; Bakkers, E. P. A. M. Diameter-Dependent Conductance of InAs Nanowires. *J. Appl. Phys.* **2009**, *106*, 124303.
- (53) Dayeh, S. A.; Yu, E. T.; Wang, D. L. Transport Coefficients of InAs Nanowires as a Function of Diameter. *Small* **2009**, *5*, 77-81.

Figures and captions

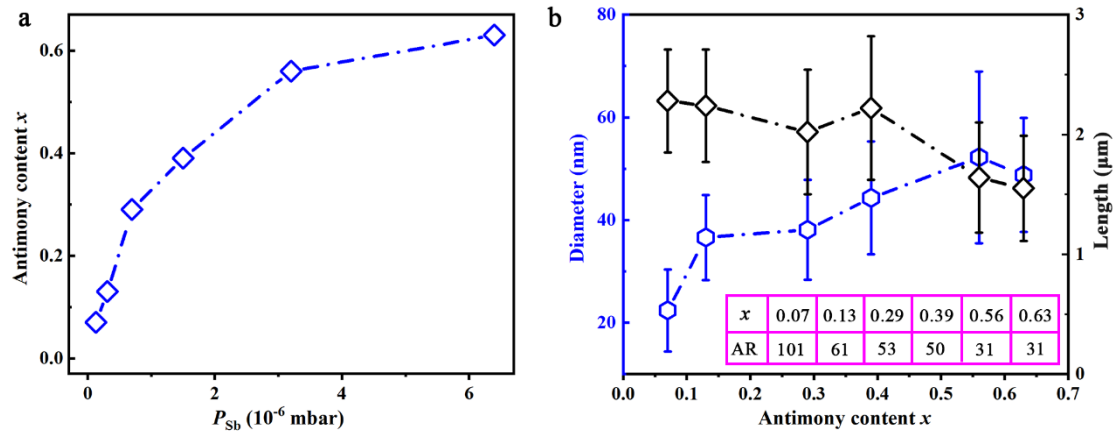


Figure 1. a) The antimony content x of $\text{InAs}_{1-x}\text{Sb}_x$ nanowires as a function of the antimony flux P_{Sb} . b) The average diameter and length of $\text{InAs}_{1-x}\text{Sb}_x$ nanowires as a function of the antimony content x . The AR of nanowires is also given in panel (b). Each data point in panel (b) is a statistical average of more than 50 nanowires.

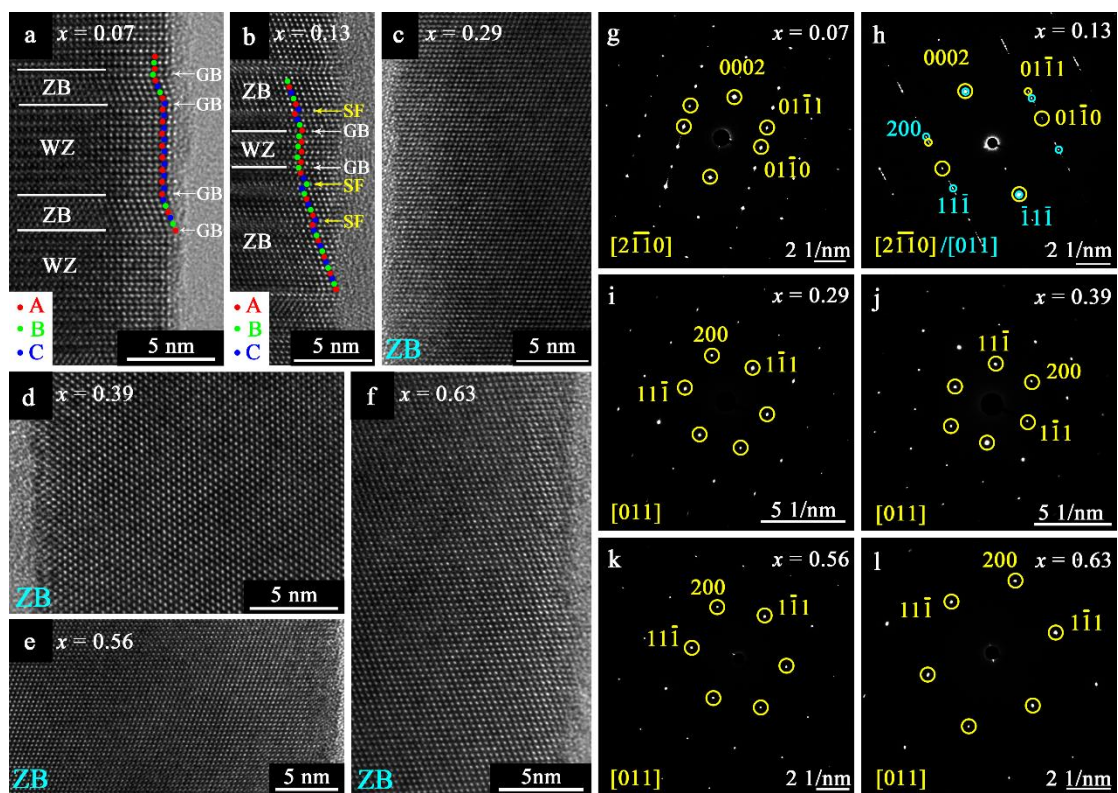


Figure 2. a-f) Typical HRTEM images of $\langle 0001 \rangle$ - or $\langle 111 \rangle$ -oriented $\text{InAs}_{1-x}\text{Sb}_x$ nanowires with x of 0.07, 0.13, 0.29, 0.39, 0.56 and 0.63, respectively. g-l) The corresponding SAED patterns of $\text{InAs}_{1-x}\text{Sb}_x$ nanowires in panel (a-f).

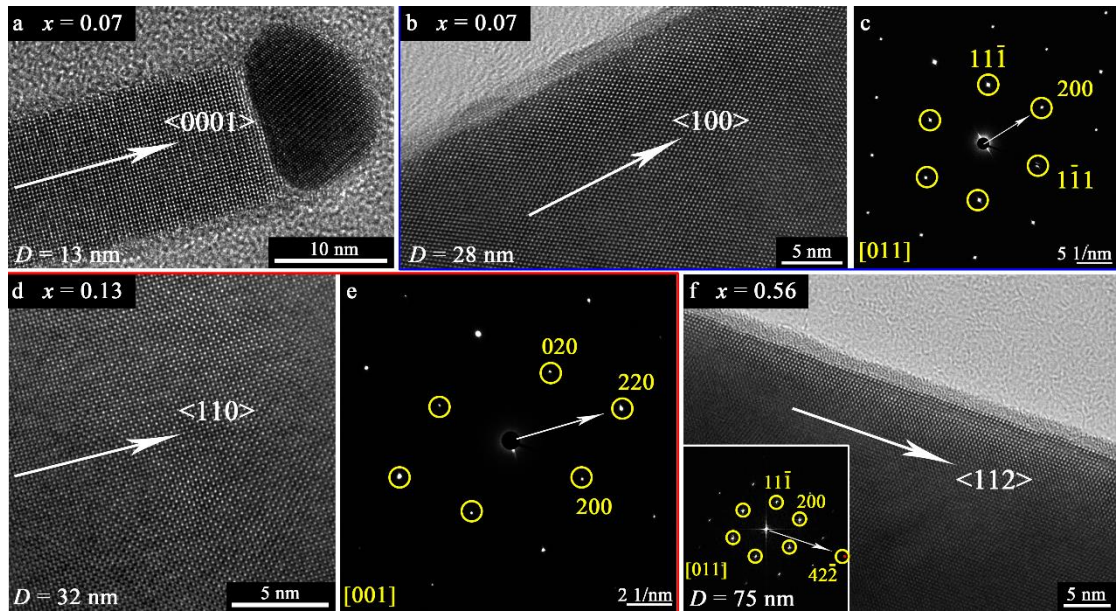


Figure 3. a) HRTEM image of the $\langle 0001 \rangle$ -oriented $\text{InAs}_{0.93}\text{Sb}_{0.07}$ nanowire with a diameter of 13 nm. b,c) HRTEM image and SAED pattern of the $\langle 100 \rangle$ -oriented $\text{InAs}_{0.93}\text{Sb}_{0.07}$ nanowire with a diameter of 28 nm. d,e) HRTEM image and SAED pattern of the $\langle 110 \rangle$ -oriented $\text{InAs}_{0.87}\text{Sb}_{0.13}$ nanowire with a diameter of 32 nm. f) HRTEM image of the $\langle 112 \rangle$ -oriented $\text{InAs}_{0.44}\text{Sb}_{0.56}$ nanowire with a diameter of 75 nm. The inset is its fast Fourier transform image.

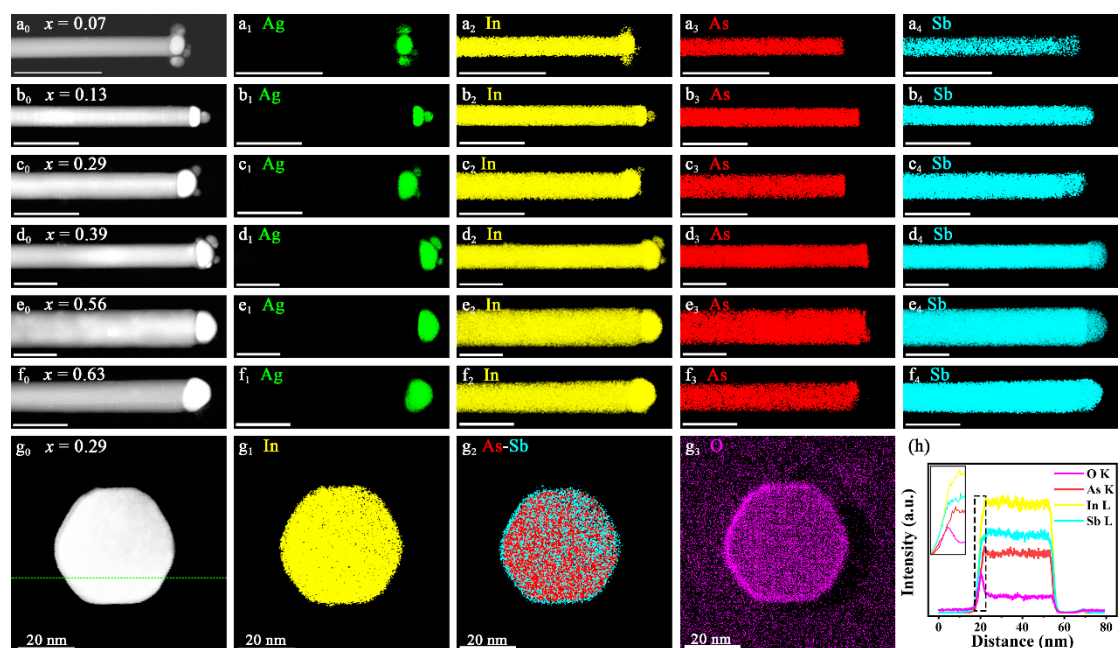


Figure 4. a₀-f₄) HAADF-STEM images and corresponding false-color EDS maps of InAs_{1-x}Sb_x nanowires with x of 0.07, 0.13, 0.29, 0.39, 0.56 and 0.63, respectively. g₀-g₃) The cross section HAADF-STEM image and corresponding false-color EDS maps of the InAs_{0.71}Sb_{0.29} nanowire. h) The EDS line scans taken along the green dotted line in panel (g₀). Scale bars in panel (a₀-f₄): 100 nm.

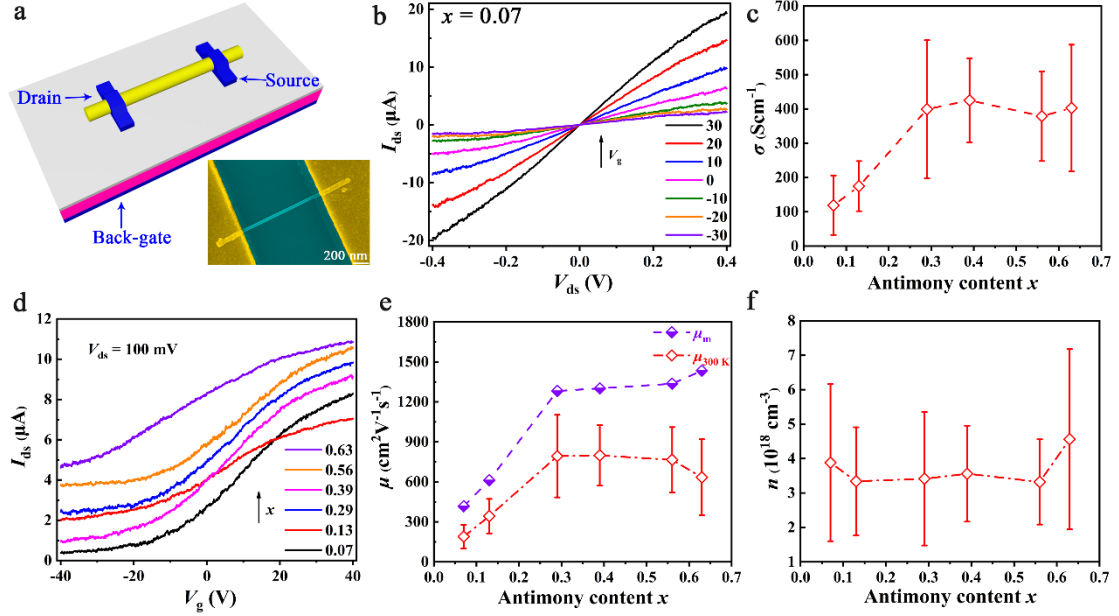


Figure 5. a) A schematic diagram and typical SEM image of the InAs_{1-x}Sb_x nanowire FET. b) Output characteristics of the InAs_{0.93}Sb_{0.07} nanowire FET at 300 K with different V_g . c) Average conductivity of nanowires as a function of the antimony content x . d) Transfer characteristics of InAs_{1-x}Sb_x nanowire FETs at 300 K. e) Average mobility ($\mu_{300\text{K}}$) and the maximum mobility (μ_m) of nanowires as a function of the antimony content x . f) Average carrier concentration of nanowires as a function of the antimony content x . Each data point in panel (d,f) is a statistical average of the electrical results of 15-25 nanowires.

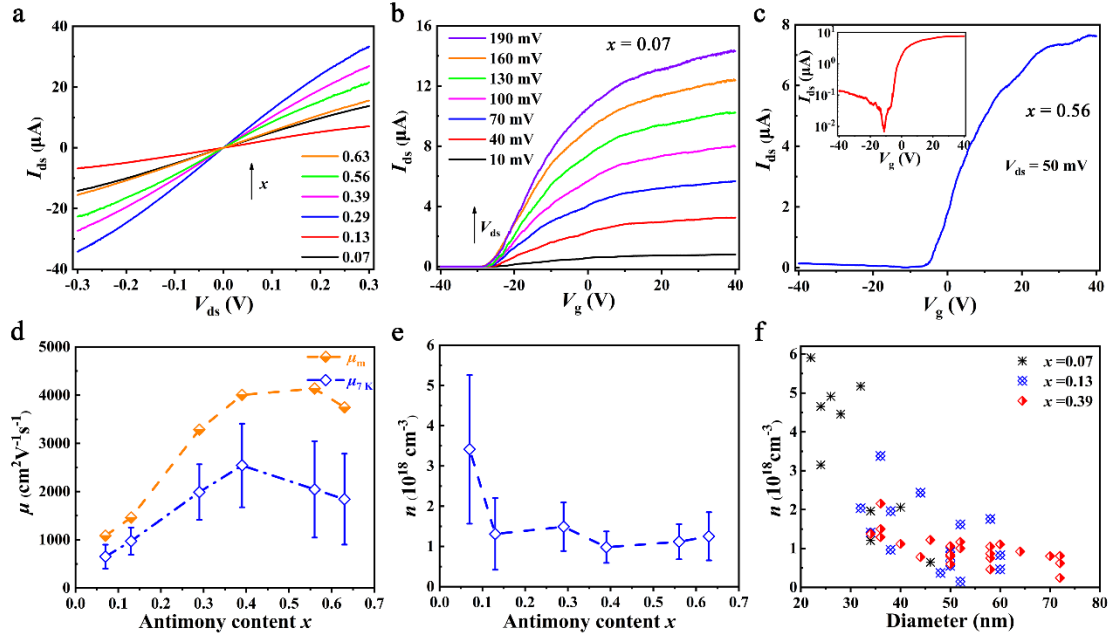


Figure 6. a) Output characteristics of InAs_{1-x}Sb_x nanowire FETs at 7 K. b,c) Transfer characteristics of the InAs_{0.93}Sb_{0.07} and InAs_{0.44}Sb_{0.56} nanowire FETs at 7 K, respectively. d) Average mobility (μ_{7K}) and maximum mobility (μ_m) of nanowires as a function of the antimony content x . e) Average carrier concentration of nanowires as a function of the antimony content x . f) Carrier concentration of nanowires with different antimony contents as a function of the diameter. Each data point in panel (d,e) is a statistical average of the electrical results of 10-25 nanowires.

Supporting Information

Large-composition-range pure-phase homogeneous InAs_{1-x}Sb_x nanowires

Lianjun Wen,^{†,‡} Dong Pan,^{*,†,‡,⊥} Lei Liu,^{†,‡} Shucheng Tong,[†] Ran Zhuo,^{†,‡} and Jianhua
Zhao^{*,†,‡,§}

[†]*State Key Laboratory of Superlattices and Microstructures, Institute of Semiconductors, Chinese Academy of Sciences, P.O. Box 912, Beijing 100083, China*

[‡]*College of Materials Science and Opto-Electronic Technology, University of Chinese Academy of Sciences, Beijing 100049, China*

[⊥]*Beijing Academy of Quantum Information Sciences, 100193 Beijing, China*

[§]*CAS Center for Excellence in Topological Quantum Computation, University of Chinese Academy of Sciences, Beijing 100049, China*

*E-mails: pandong@semi.ac.cn; jhzhao@semi.ac.cn

Contents

S1 Large-composition-range InAs_{1-x}Sb_x nanowires grown on Si (111) substrates

S2 Compositional distribution in the cross section of InAs_{1-x}Sb_x nanowires

S1 Large-composition-range InAs_{1-x}Sb_x nanowires grown on Si (111) substrates

Figure S1 shows SEM images of InAs_{1-x}Sb_x nanowires with different antimony contents grown on Si (111) substrates by MBE. We can see that <111>- and non-<111>-oriented nanowires coexist on the surface of Si (111) substrates. With increasing the antimony content x , the density of nanowires begins to gradually decrease. This phenomenon can be understood by the fact that a high antimony flux is detrimental to nanowire growth.¹

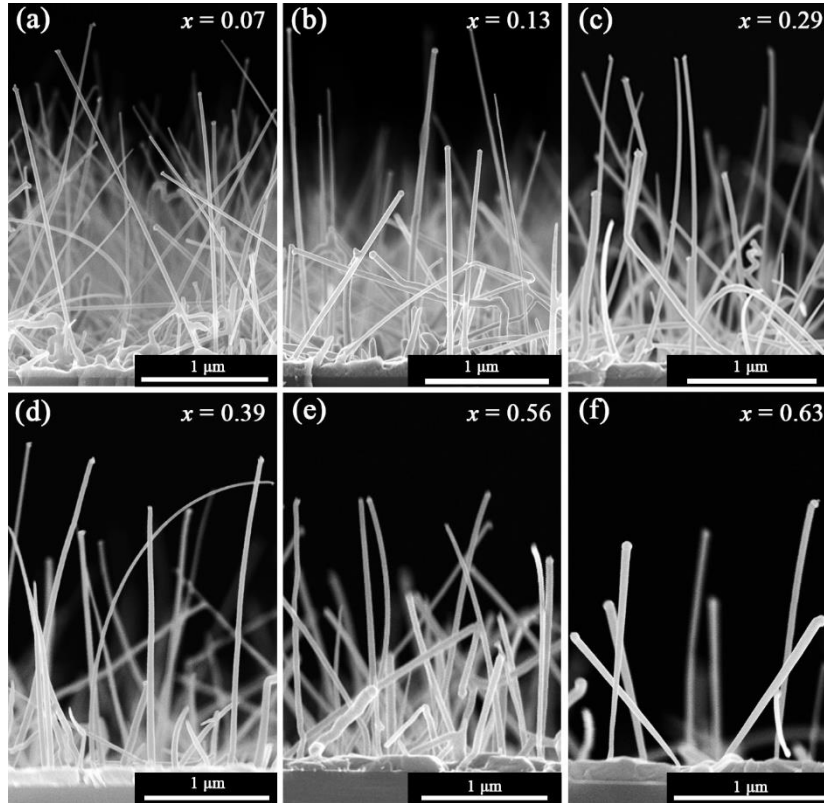


Figure S1 (a-f) Typical side-view SEM images of InAs_{1-x}Sb_x nanowires with the antimony content x of 0.07, 0.13, 0.29, 0.39, 0.56 and 0.63, respectively.

S2 Compositional distribution in the cross section of InAs_{1-x}Sb_x nanowires

Figure S2 shows cross section HRTEM images and corresponding EDS maps of InAs_{1-x}Sb_x nanowires. We can see that there are no planar defects in pure ZB phase nanowires. The corresponding EDS maps indicate that the indium, arsenic and antimony are uniform across the cross section, and no obvious vapor-solid growth is observed on the sidewalls of the nanowire.

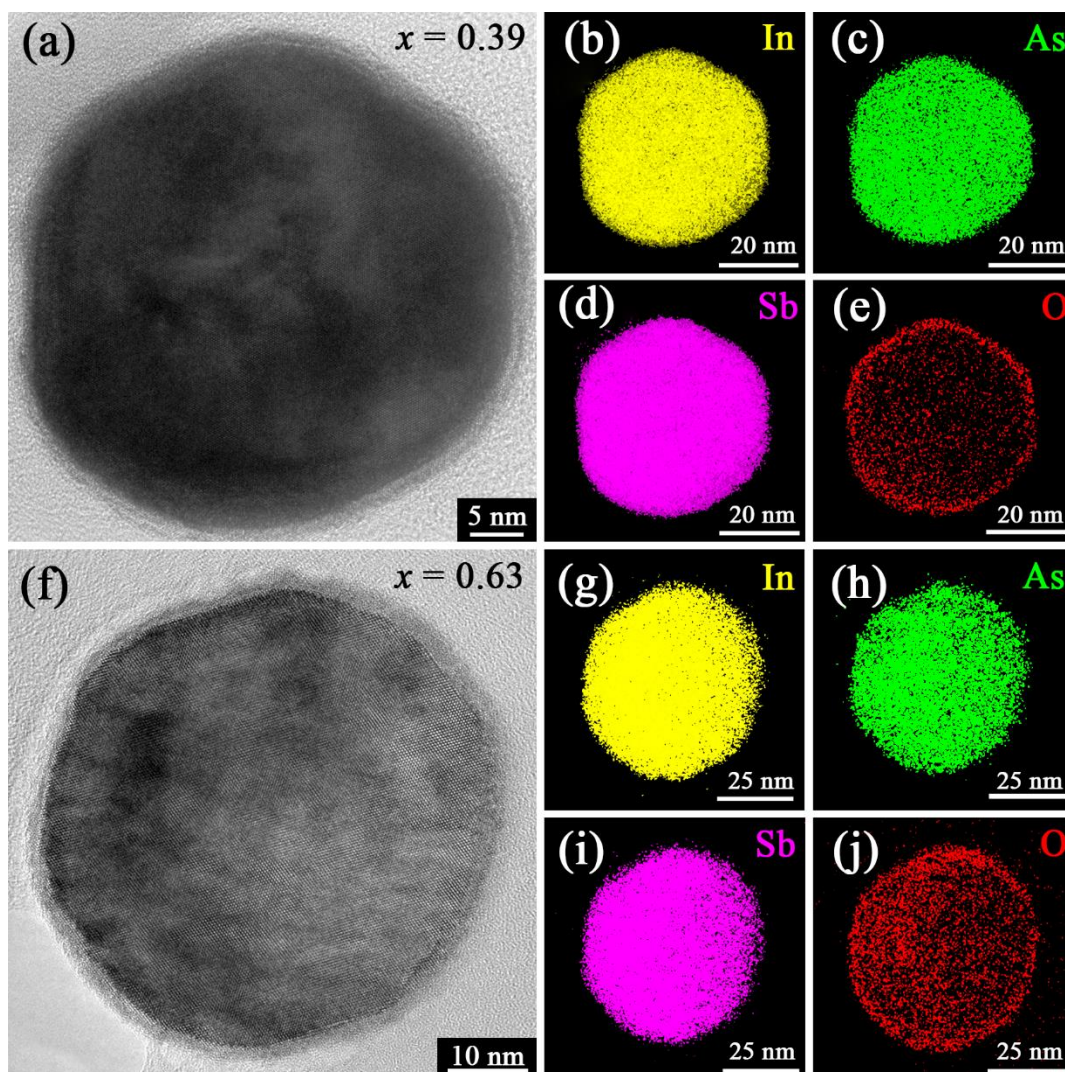


Figure S2 (a-e) Cross section HRTEM images and EDS maps of the $\text{InAs}_{0.61}\text{Sb}_{0.39}$ nanowire. (f-j) Cross section HRTEM images and EDS maps of the $\text{InAs}_{0.37}\text{Sb}_{0.63}$ nanowire.

Reference

- (1) Sourribes, M. J. L.; Isakov, I.; Panfilova, M.; Liu, H. Y.; Warburton, P. A. *Nano Lett.* **2014**, *14*, 1643.